Journal of Biomedical Optics

BiomedicalOptics.SPIEDigitalLibrary.org

Cherenkov luminescence imaging in transparent media and the imaging of thin or shallow sources

Sergey Komarov
Dong Zhou
Yongjian Liu
Yuan-Chuan Tai

SPIE.

Cherenkov luminescence imaging in transparent media and the imaging of thin or shallow sources

Sergey Komarov,* Dong Zhou, Yongjian Liu, and Yuan-Chuan Tai
Washington University in St. Louis, Department of Radiology, 510 S. Kingshighway Boulevard, Campus Box 8225, St. Louis, Missouri 63110, United States

Abstract. In this work, we demonstrated the possibility of high spatial resolution Cherenkov luminescence imaging (CLI) for objects in transparent media. We also demonstrated the possibility of the CLI of thin opaque objects using optical transducers. Results demonstrate that submillimeter resolution CLI is achievable for beta-emitting radionuclides, including ^{76}Br that emits positrons of very high energy. The imaging of beta-emitters through scintillation detectors exhibits lower resolution when compared to CLI of the same sources. The application of optical transducers for the CLI was demonstrated using plants labeled with $^{11}CO_2$ and phantoms containing beta-emitters. [DOI: 10.1117/1.JBO.20.3.036011]

Keywords: Cherenkov luminescence imaging; nuclear imaging.

Paper 140835R received Dec. 15, 2014; accepted for publication Feb. 25, 2015; published online Mar. 19, 2015.

1 Introduction

Cherenkov luminescence imaging (CLI) has recently become a standard tool for biological studies that use beta-labeled biomarkers.[1–10] The simplicity of CLI, its relatively low cost, and the ability to conduct of high-throughput screening (multiple mice can be imaged in only a few minutes) make it more advantageous than other nuclear imaging techniques [single-photon emission computed tomography or positron emission tomography (PET)]. More importantly, CLI enables *in vivo* imaging of pure beta-emitting radionuclides (such as ^{32}P) that were previously believed to be only suitable for *in vitro* imaging studies using conventional beta instrumentation designed to image thin tissue samples. A disadvantage of CLI is that it is best suited for small animal imaging applications because light photons are absorbed and significantly scattered by biological tissues. For this reason, CLI has been considered a convenient but low resolution and nonquantitative imaging technique.

Despite this perception, CLI has the potential to provide high resolution images of beta-emitter distribution under specific imaging conditions. Here, we show CLI of transparent media and CLI of shallow sources and demonstrate the possibility of submillimeter resolution CLI. In addition, we demonstrate the "flashlight effect" (described below) and have investigated the use of optical transducers for CLI enhancement. As an example, we present the CLI images of photosynthetic ^{11}C assimilation in plants.

An IVIS Lumina II XR System (Caliper Life Sciences, now PerkinElmer) was used for all our experiments–this is an optical imaging system widely used by the molecular imaging research community. All images were obtained with a 5-min acquisition time and with the highest resolution [IVIS imaging table position: field of view (FOV) "A"] unless it is stated otherwise.

*Address all correspondence to: Sergey Komarov, E-mail: komarovs@mir.wustl.edu

2 Flashlight Effect

CLI is an imaging technique based on the Cherenkov effect, first reported by Pavel Cherenkov in 1934, which is the emission of electromagnetic radiation by a charged particle moving through a medium faster than the phase velocity of light in that medium.[11,12] In transparent media, the radiation emitted per unit time by a particle with a charge q is given by the Frank-Tamm equation[13]

$$\frac{dW}{dt} = \frac{q^2\beta}{c}\int_{n(\omega)\beta>1}\left(1-\frac{1}{n(\omega)^2\beta^2}\right)\omega d\omega,$$

where $n(\omega)$ is the media's index of refraction for radiation frequency ω and β is the particle velocity in the unit of speed of light. The Cherenkov radiation (CR) is emitted at specific angle θ relative to the particle velocity vector given by $\cos\theta = [n(\omega)\beta]^{-1}$.

A group of particles of various energies moving in the same direction will emit light within a cone, the geometry of which resembles that typically seen by shining a flashlight in the dark. We use the term "flashlight effect" throughout this work to refer to this unique pattern. In the absence of light scattering, the only CR that can pass through the lens system and be detected [see Fig. 1(a)] is the CR of the particles traveling toward the camera within the angle φ_{max}; this angle is determined by the camera angular aperture Ω and the maximum angle θ of the CR (determined by the end-point energy of the radionuclide). It should be noted that high-energy beta particles traveling toward the camera may be undetected if the CR is emitted along a large θ ($\theta > \Omega/2$), where the CR emission cone completely misses the camera aperture.

Forward-oriented CR radiation has three interesting aspects relevant to imaging applications. First, since only particles that move toward the camera can contribute to the CLI image, the maximum width of the point spread function (PSF) is

1083-3668/2015/$25.00

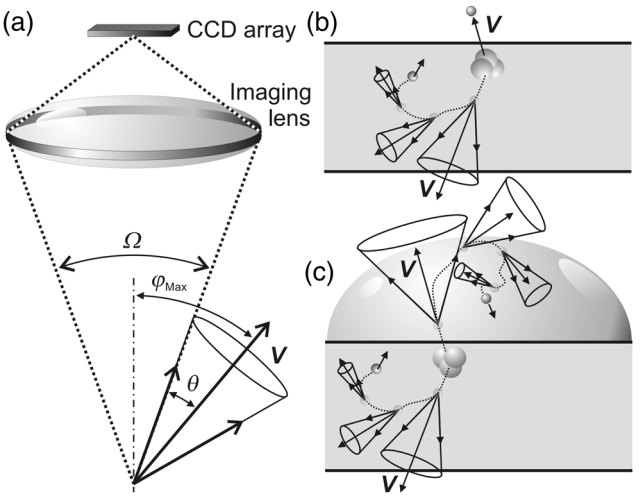

Fig. 1 Cherenkov luminescence imaging (CLI) using an optical charge-coupled device (CCD) camera: (a) "flashlight effect" in transparent medium–only the Cherenkov radiation (CR) produced by the particles moving toward camera (within angle φ_{max}) can be detected; (b) "shallow" source–no CR can be emitted toward camera since there is no media above the source; (c) "shallow" source covered with a high index of refraction optical transducer–CR is produced in the transducer to enable detection of the shallow source.

determined not by the particle's range (as in PET) but by the CR particle range scaled by the factor $\sin \varphi_{max} < 1$ (i.e., by the projection of the particle range onto the imaging plane). Second, the PSF is additionally sharpened because more CR is emitted at the beginning of the particle's trajectory where the particle velocity is the highest (this means that the "effective" CR emission range will be shorter than the actual range of the particle). Therefore, there is less blurring due to the beta particle's range. Third, if the range of the beta particles is large enough to allow some particles to escape from the object's surface, those particles can be harnessed using transparent transducers with a high index of refraction [as illustrated in Figs. 1(b) and 1(c)] to further increase the light output, thus theoretically improving resolution.

From the Frank-Tamm equation, it can be seen that the CR emission has a continuous spectrum that is heavily weighted in the UV and blue range. In the UV region ($\lambda < 400$ nm), the dispersion of light in media can be significant. However, most optical imagers (including the IVIS) employ charge-coupled device (CCD) sensors that have low-quantum efficiency in the UV region. Most optical lenses used in these systems also strongly absorb UV light. As a result, most CR signals that can be detected by common optical imagers are visible light photons. In the visible light region, the indices of refraction of acrylic are 1.5 and 1.49 for photons of 400 and 700 nm wavelengths, respectively. The corresponding values for water are 1.34 and 1.33, respectively. Given the above considerations, the dispersion of CR light is insignificant (<1%) for the applications described in this work.

3 Resolution of Cherenkov Luminescence Imaging

Although the resolution of CLI is related to the range and energy of particles, the "flashlight effect" suggests that the resolution of CLI can be much better than the resolution determined solely by the range of beta particles. To demonstrate the possibility of high resolution CLI and the dependence of resolution on the beta particle's energy, we evaluated CLI images of two point sources–^{18}F (mean and end-point energies are 0.25 and 0.63 MeV) and ^{76}Br (mean and end-point energies are 1.18 and 3.94 MeV). An acrylic plate (5.3-mm thick; 1.19 g/cm^2; $n = 1.5$) was placed over the sources as a transducer to produce CL images. The CR emission angles in acrylic at the mean (end-point) energy are: 25 deg (42 deg) for ^{18}F; and 46 deg (48 deg) for ^{76}Br, respectively. Luminescent images of the same two point sources were also obtained with a BC408 plastic scintillator screen (4.7 mm thick) and compared with CL images from the transducer.

The setup of the experiments for both sources was similar: a point source (~1 mm in diameter) on the surface of a 1.8-mm thick acrylic plate was covered with: (1) the acrylic transducer and (2) the BC408 scintillator screen. There was a small air gap (~0.04 mm) between the unsealed surface source and the transducer (or scintillator) plate to avoid radioactive contamination from direct contact. Since the same unsealed source was used in two consecutive experiments, the experiments were repeated to guarantee that the unsealed source had not been disturbed between experiments. Decay-corrected results for ^{18}F and ^{76}Br are presented in Figs. 2 and 3.

Despite the strong differences in light outputs between the acrylic transducer and scintillator (the ratios of max radiance in the scintillator to max radiance in the acrylic transducer were ~40 for ^{18}F and ~16 for ^{76}Br), the acrylic transducer demonstrated a smaller full width at the half maximum (FWHM) than the BC408 scintillator. For a ^{76}Br source, the impact of this improvement in resolution is more obvious if one considers the full width at the tenth maximum: 5.6 mm for the scintillator versus 3.2 mm for the acrylic transducer.

For high-energy beta emitters (such as ^{76}Br), the "flashlight effect" can potentially create a blind spot in images–the CR cone from particles that move toward camera cannot be detected when the cone angle is larger than the angular dimension of the camera aperture. This effect can be clearly seen if (1) the CR radiation that comes from the vicinity of the source is blocked and (2) only the radiation from the transducer may

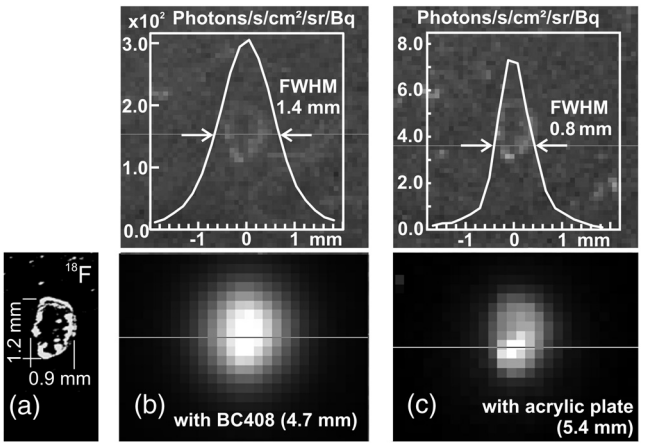

Fig. 2 ^{18}F source (100–80 kBq) on an acrylic plate: (a) microscope image of the source in incident illumination; (b) IVIS luminescent image of the source through the BC408 scintillator; (c) IVIS CLI image of source through an acrylic transducer. Corresponding decay-corrected radiance profiles above each image are aligned with the image below. Images (a), (b), and (c) are horizontally aligned. All images are presented in the same scale.

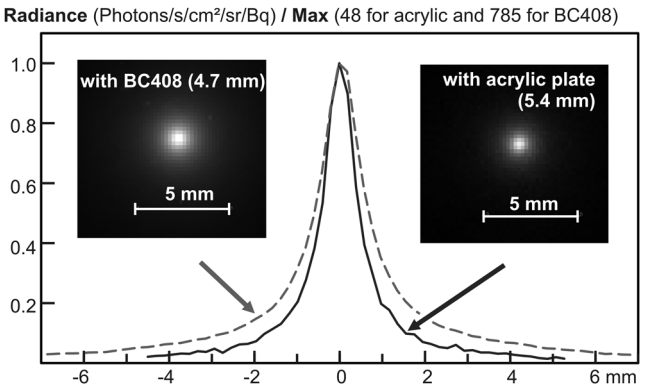

Fig. 3 Radiance profiles of the ^{76}Br (~20 kBq) source covered with the acrylic transducer [solid line: full width at the half maximum (FWHM) = 0.9 mm] versus covered with the BC408 scintillator screen (dashed line: FWHM = 1.3 mm).

be detected (see Fig. 4). In Fig. 4, (S) is a beta source; (a) is a spacer or some media in which CR (photon group 1) can be produced but it is blocked by a nontransparent screen (c); (b) is a transducer. The beta particles (solid lines) that enter the transducer (b) produce CR (dashed lines in groups 2 and 3). High-energy betas that travel directly toward the lens will emit CR (group 3) along a cone with a large angle θ and as such will miss the camera aperture. In contrast, CR from high-energy betas that travel at a direction off the central axis of the optical lens (group 2) will be collected and contribute to the CL images. If the direction of beta particles does not change significantly as they pass through the media (a), and there are sufficient numbers of high-energy beta particles with a mean energy that is high enough to penetrate media (a) and still produce CR at large θ angle, a distinct ring around the source S should be seen in the CLI.

We set up two experiments to demonstrate and characterize this "ring artifact." In these experiments, a double ^{76}Br source (two point sources ~0.5 mm in diameter separated by 1 mm) was used. The source was planted on the surface of a 1.8-mm thick acrylic plate and sealed by transparent tape (7.7 mg/cm^2 and 0.04 mm thick). Experiments were conducted with two source orientations relative to the IVIS camera: (1) "normal"–source on the top of the plate (Fig. 5) and (2) "flipped"–source on the bottom of the acrylic plate (Fig. 6). In terms of Fig. 4, the only difference between these two experiments is the spacer (a): in "normal" setup, the spacer is a thin transparent tape; in "flipped" setup, the spacer is a 1.8 mm acrylic plate. Three images were obtained for both experiments. The first was the image of the source only (labeled as "blank", where either the transparent tape or the acrylic base

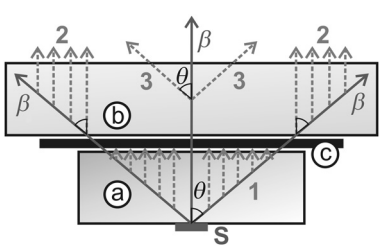

Fig. 4 CR ring formation in CLI with optical transducers: S is a beta source; (a) is a spacer or media; (b) is a transducer; and (c) is a black screen.

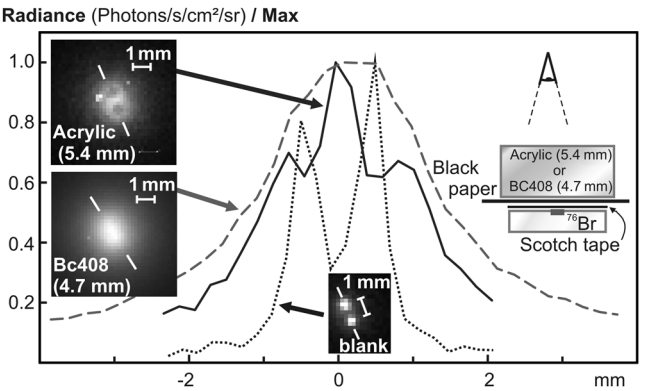

Fig. 5 Luminescent images and corresponding normalized radiance profiles of double ^{76}Br sources: (1) dotted line–sources are covered by a thin transparent media (Scotch tape) only (self-normalized with a scale of Max = 2.19×10^5); (2) solid line–source covered by a tape, a piece of black paper and an acrylic transducer (self-normalized with a scale of Max = 2.6×10^5); (3) dashed line–source covered by a piece of black paper and scintillator BC408 (self-normalized with a scale of Max = 5.0×10^7). Positions of radiance profiles are shown on luminescent images by white lines.

plate acts as a transducer). The other two are the images of the source covered with black paper (0.1 mm thick) obtained through either: (1) the thick acrylic transducer plate or (2) the BC408 scintillator screen. Experiment configurations are inset on the right side of Figs. 5 and 6.

Results in Figs. 5 and 6 clearly demonstrate submillimeter resolution CLI capacity when the sources are directly under a transparent transducer, despite the fact that the beta source has very high end-point energy (such as ^{76}Br). Two point sources that are separated by 1 mm can be clearly delineated in the images labeled as "blank." When a piece of black paper blocks off the CL from the spacer transducer, the "ring" artifact around the sources (as described in Fig. 4) can be clearly seen.

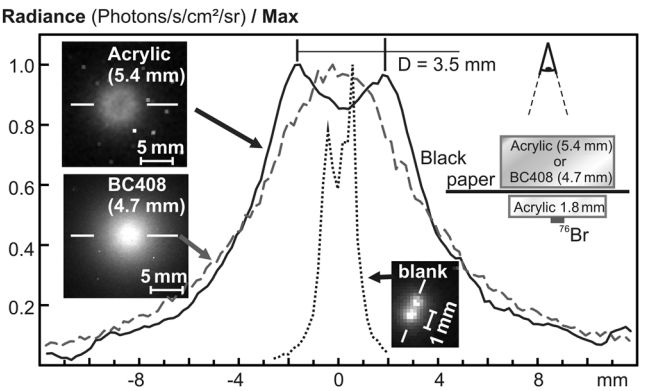

Fig. 6 Luminescent images and corresponding normalized radiance profiles of the "flipped" ^{76}Br source: (1) dotted line–CLI image of the source on the bottom of the acrylic base plate (self-normalized with a scale of Max = 8.0×10^5); (2) solid line–source on the bottom of the acrylic plate covered by black paper and acrylic transducer (self-normalized with a scale of Max = 2.7×10^4); (3) dashed line–source on the bottom of the acrylic plate covered by black paper and scintillator BC408 (self-normalized with a scale of Max = 7.6×10^5). Note that a low-pass filter (3 × 3 pixels averaging) was applied to the image with acrylic transducer to reduce the statistical noise.

As was noted before, the "ring artifact" and "blind spots" can only be seen under the following special conditions: (1) the CR emission from the initial trajectory of the source is blocked off (such as that shown in Fig. 4). Otherwise, the density of the CR emission near the point source will dominate and the blind spot will not be visible. (2) There is a significant fraction of beta particles that move toward the imager with high energy. In Fig. 4, we illustrated the formation of a blind spot from high-energy betas. For those betas that move directly toward the imager (group 3), the CR is emitted at a large angle and will not be collected by the lens. However, if there is a significant fraction of betas with lower energy, their CR emission will be at a smaller angle and can fill in the blind spot. The diameter of the blind spot (formed by beta particles labeled as group 2 in Fig. 4) depends on the energy of the beta particles (higher energy, larger angle θ, and larger diameter). For ^{76}Br, the blind spots are easily observable because its high-energy betas have a range of up to 2 cm (for acrylic the stopping power is ~2 MeV/cm). While betas slow down as they travel through the acrylic transducer, many of them remained energetic even when they escape the transducer (5 mm thick) and their emission angles remained large and do not contribute to the collected signals. (Notice the small difference between the mean and max emission angles for ^{76}Br described earlier.) As a result, the blind spots are not completely filled in by CR emission from lower energy betas (either betas that were emitted with low energies or those that started out with high energies and slowed down as they traveled). Consider the mean and max (mean/max) energies of beta particles from ^{18}F and ^{11}C to be 250/630 and 385/960 keV, respectively. In acrylic ($n \sim 1.5$), these energies correspond to emission angles of ~25 deg/42 deg and 36 deg/44 deg, respectively. In principle, one should be able to observe blind spots from ^{18}F and ^{11}C. However, if we set up the same experiment using ^{18}F or ^{11}C, the diameter of the blind spots would be smaller to start with. More importantly, many betas will be at lower energies and emit CR at a wide range of angles. As a result, these signals will contribute to the collected signal by the CCD and fill in the blind spots to make them easily invisible.

The "flashlight effect" can be also demonstrated in another simple experiment. Compare three CLI images of a beta-emitter point source on the surface of an acrylic plate: (1) source on the top of the plate; (2) the same source covered with transparent tape; and (3) "flipped" source-source imaged through the acrylic plate. With the "flashlight effect," we can respectively expect the following for CLI images of these sources: (1) minimal CR light output (since it can be produced only by back-scattered particles or reflected photons) and thus, the worst resolution; (2) median light output and high resolution (due to the short range of particles in thin media); and (3) the largest light output with the median resolution (the large range of the particles maximizes the CR output but slightly degrades the image resolution). As an example, we can compare these predictions with corresponding radiance profiles of CLI images of ^{76}Br source (0.6 MBq; ~1 mm diameter) on the surface of a 1.8-mm thick acrylic plate (see Fig. 7).

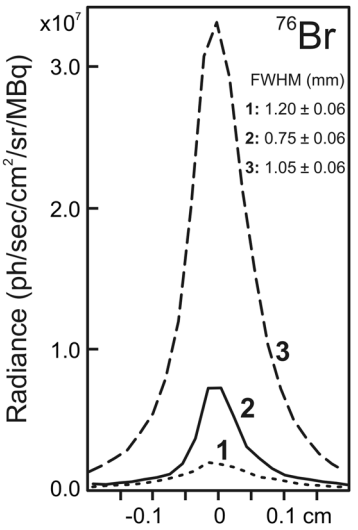

Fig. 7 Radiance profiles of ^{76}Br source: (1) source is on the top of 1.8-mm thick acrylic plate (dotted line 1); (2) the same source sealed by thin (~0.04 mm) tape (solid line 2); and (3) "flipped" source (dashed line 3)–source on the bottom of the plate. Corresponding FWHM is shown in a plot.

4 Cherenkov Luminescence Imaging of Plants

The radionuclide ^{11}C is a pure positron emitter with a short half-life (20.3 min). The short half-life of ^{11}C and the important role of carbon in biological processes make ^{11}C a convenient tool for dynamic studies of photosynthesis and carbon translocation processes in plants. The energy of positrons emitted from ^{11}C (the mean and end-point positron energies are 0.39 and 0.96 MeV) is sufficiently high for CLI (the energy threshold for CR in water is 260 keV). The corresponding Cherenkov angles for water are: 24 deg (37 deg). Unfortunately, plant leaves are strongly phosphorescent in comparison with the weak CR signal, which adds challenges to the use of CLI on plant imaging applications. Despite these limitations, plant roots are not phosphorescent. Very little light propagates from the leaves to the roots either through the soil or through the stem. To enable root imaging, the plant should be grown in a container in which either the roots grow along a transparent window[14] or in a transparent substrate.[15] The most convenient technique for CLI of root architecture is a plant grown in transparent gel. We have conducted CLI of plant roots using both scenarios: an opaque substrate with roots grown against the glass window [Fig. 9(a)] and using a transparent gel as a substrate (Fig. 8). The glass window technique has an obvious disadvantage: because only a portion of the roots grow adjacent to the window, the resolution and sensitivity of CLI are limited by the distance between the window and those roots. The intensity of CR produced in very thin roots is small, thus for CLI the roots need to be surrounded by a transparent media (water) that is used as a transducer. As a result, the best results in our experiments were obtained when the roots were grown in transparent gel. Optically clear gels are widely used as substrates for the studies of root architecture in other imaging modalities.[15–17] Here, we present only the CLI results of a young cucumber plant grown in gellan gum (see Fig. 8). The plant was exposed to 100 MBq $^{11}CO_2$ gas in an ~0.2 L uptake chamber for 0.5 h and images were obtained 1 and 6 h later [Figs. 8(a) and 8(b)]. Figure 8(b) demonstrates the contribution from the phosphorescent light. After 6 h, there is no remaining radioactivity and only phosphorescent light contributes to the luminescent image (the ^{11}C is presumed absent after ~18 half-lives). A comparison of Figs. 8(a) and 8(b) indicates that the luminescence in roots in 8(a) is mostly due to CR.

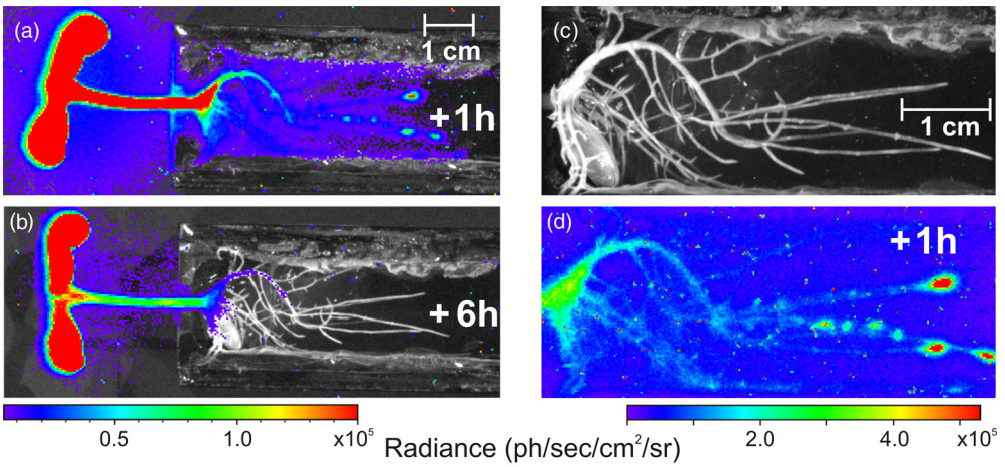

Fig. 8 CLI and optical images of young cucumber plant labeled with $^{11}CO_2$: (a) 1 h after labeling–phosphorescence + CR; (b) 6 h after labeling–phosphorescence only; (c) photograph and (d) corresponding high resolution CLI image of the roots.

Figures 8(a) and 8(b) were obtained with a 5-min acquisition time using the same FOV (IVIS FOV "C"). The high resolution CL image acquired with a 10-min acquisition time and the IVIS FOV "A" is presented in Fig. 8(d). Figure 8(c) is a reference photographs of the object presented in Fig. 8(d). A line profile drawn across the hot spots in the CL image in Fig. 8(d) shows that a resolution of ~0.5 mm (0.6 to 0.8 mm FWHM measured from roots of 0.3 to 0.5 mm diameters) is achievable when using ^{11}C in transparent media.

Despite the strong phosphorescent signal from the leaf and stem, the distribution of ^{11}C in the leaves can be visualized by CLI using a transparent transducer with a thin black plastic screen. The black screen blocks all optical radiations but not the high-energy beta particles which escape the thin surface of the leaf. The escaped particles induce CR in the transparent transducer, producing a CLI image that represents the distribution of escaped beta particles from a leaf. The resolution of the image in this scenario will depend on the distance between the transducer and leaf surface. We expected the "flashlight effect" would minimize blurring due to the angular selection of the beta particles. For this reason, we did two experiments: (1) *in vivo* image of the leaf (top side)–the transducer was placed as close as possible to the leaf's upper surface while avoiding leaf damage and (2) *in vitro* image of the leaf (bottom side)–leaf was detached from the plant and pressed firmly (to compress all possible air gaps between leaf and transducer) along the transducer surface.

The setup and results of experiments are presented in Fig. 9. Figure 9(d) shows an *in vivo* image of the upper surface of a cucumber leaf (1) after it was exposed to $^{11}CO_2$ (370 MBq in a chamber of ~1 L in volume) for 15 min; the image was obtained with a 12-mm thick acrylic transducer (3) placed above a thin opaque black plastic sheet (2) which blocks the phosphorescent light. Bicron BC630 optical grease was used to fill the possible gaps between the transducer and the thin black plastic sheet in these experiments. Total plant uptake

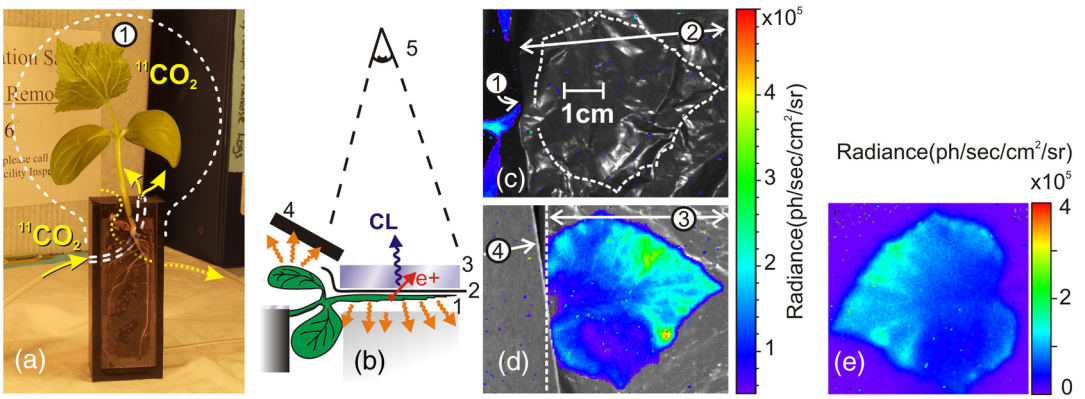

Fig. 9 Plant imaging experiment: (a) a young cucumber plant labeled with $^{11}CO_2$ gas (370 MBq for 15 min in ~1 L chamber); (b) CLI setup: a thin black plastic sheet (2) blocks phosphorescent light from the imaged leaf (1); an acrylic transducer 12 mm thick (3) is placed over the leaf; an additional black paper screen (4) blocks phosphorescent light outside the imaging field of view (FOV); (5) is a CCD camera; (c) CLI of the leaf (1) covered by thin black plastic sheet (2) without transducer; (d) CLI of the same leaf with transducer (3); (e) CLI of detached and flipped leaf. The optical grease Bicron BC 630 was used between (2) and (3) to press the plastic sheet to the leaf surface and fill the gap between the flat transducer and the plastic sheet. (d) and (e) are obtained 18 and 36 min after the labeling.

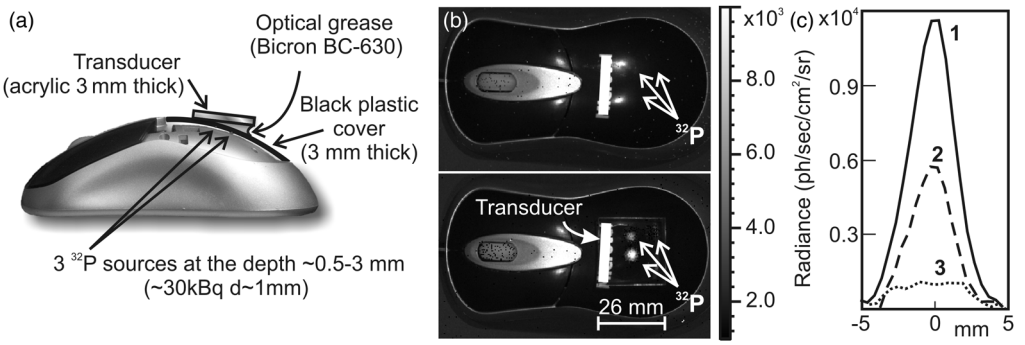

Fig. 10 CLIs of nontransparent curved plastic object with three ^{32}P sources planted on the bottom of the curved black plastic plate at the depths of 0.5 to 3 mm: (a) experiment setup; (b) top image is CLI without transducer, bottom image is CLI with transducer; and (c) the radiance profiles of the sources.

was estimated to be ~37 MBq. The image of the leaf was obtained 18 min after labeling with a 5-min acquisition time. Figure 9(c) demonstrates that the black plastic sheet completely blocks light emission from the leaf (some emission from the plant not covered by the sheet can be seen on the left edge of the figure). A clear uptake pattern was observed in Fig. 9(d) when the acrylic transducer was placed above the opaque black plastic sheet.

Because the stem and prominent veins limit direct contact between the leaf and the transducer, the leaf was cut from the stem and imaged again. The cut leaf was flipped (veins up) to image while pressed strongly through the black plastic sheet against the acrylic transducer which had been coated with optical grease. The CLI of this leaf *in vitro* is presented in Fig. 9(e). Figures 9(d) and 9(e) are obtained in 18 and 36 min after the radio-labeling, respectively.

5 Discussion and Conclusion

The radiance profiles presented in Fig. 7 demonstrate that most of the CR light is emitted inside the acrylic plate. If we take into account Fresnel reflection from the opposite side of the acrylic plate (more than 3.8% should be reflected due to the difference in indices of refraction) and also diffuse reflection from the black paper used on the IVIS imager table (up to ~10% of incoming visible light can be reflected[18]), we can conclude that most of the light detected in profile 1 is the result of reflection and scattering of the light from a strong CR source (see profile 3) and that the CR from scattered positrons [as shown in Fig. 1(b)] is very small.

The same conclusion can be drawn from the comparison of the radiance profiles of the pure double ^{76}Br source (dotted lines in Figs 5 and 6). In both cases, most of the light is also emitted inside the acrylic plate. The maximum radiance for the "normal" source position (where the only media for CR production is a 0.04-mm thick transparent tape) is 2.2×10^5 photons/sec/cm^2/str (see dotted line in Fig. 5), while for the "flipped" source (where CR is produced in the 1.8-mm thick acrylic plate) the maximum radiance is 8.0×10^5 photons/sec/cm^2/str (see dotted line in Fig. 6).

These experiments also demonstrate that the resolution of CLI for point sources in transparent media can be significantly better than the particle range (that is up to ~2 cm for ^{76}Br and ~2 mm for ^{18}F and ^{11}C). This is a clear advantage over PET whose resolution strongly depends on positron range. Furthermore, the resolution is determined not only by the particle's energy but also by the thickness of the material. The small thickness of the tape and the "flashlight effect" ensures that the radiance profile of a source covered by tape will be very close to the actual source activity distribution. The dependence of resolution on beta particle range was not as strong as one might expect. Although the ability to resolve two sources imaged through a thin transparent tape transducer (see dotted line profile in Fig. 5) was not surprising, the ability to resolve double ^{76}Br source using a 5-mm thick transducer was less obvious. In the image of the "flipped" source presented on Fig. 6 (dotted line profile), the two ^{76}Br sources separated by 1 mm can still be easily resolved.

At the first glance, the use of transducers may not appear significant: in fact, the transducer acts as a low sensitivity beta imager. Nevertheless, this approach offers some advantages compared with conventional beta imagers. First, a transducer can be used as complementary equipment for regular CLI: it can press the object to reduce its thickness, it can flatten the object's surface, and it can improve the optical contact, thus, increasing light output. Second, transducers used with optical grease (which also acts as a transducer) provide much better contact with uneven surfaces than any conventional beta imager. An example of improvements due to the use of optical grease is presented in Fig. 10: this is the result of CLI of three ^{32}P point sources (~30 kBq; mean and end-point energies of electrons are 0.7 and 1.7 MeV) planted on the backside of a black plastic plate that has a curved surface (the gap between the flat transducer and plate varies from 0 to ~5 mm). As can be seen, there is no CR without a transducer, but when the transducer is used together with optical grease on the plate surface, all three sources are clearly visible. The difference in source radiance corresponds to the source depth in the plastic plate.

We also expect higher resolution for CLI using a transducer compared with a luminescent image using a scintillator. First, for transparent objects–while the resolution of the images with a scintillator will degrade with a distance between the source and scintillator, the CR is coming directly from the media around the source. Second, the light emission from the scintillator is mostly isotropic, and this light is produced along almost the whole trajectory of the beta particle. The comparison of images obtained with an acrylic plate and with a scintillator is shown in Fig. 11. Those are the luminescent images of a grid drawn on black paper using radioactive (^{18}F) ink. As can be seen in this figure, all grid lines can be visually resolved in the CL image obtained with an acrylic transducer while the scintillator can separate only the grid lines spaced more than 1.6 mm apart.

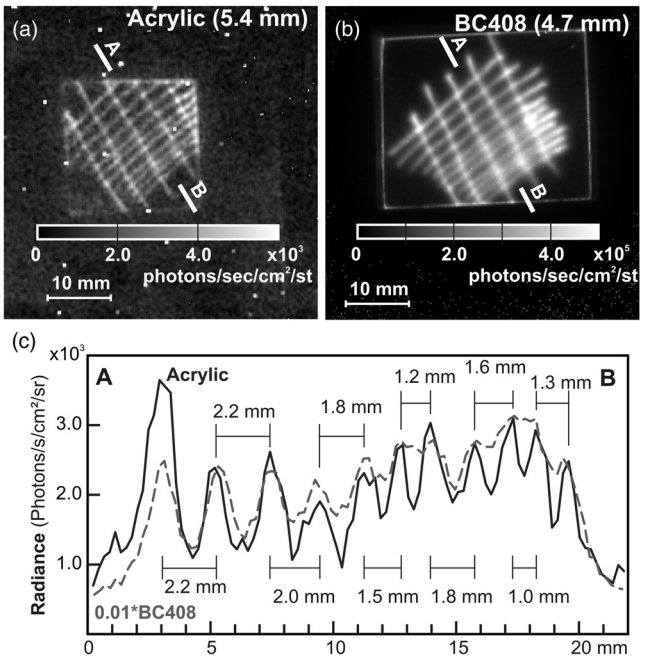

Fig. 11 (a), (b) Luminescent images and (c) corresponding radiance profiles of the grid drawn with ^{18}F ink on black paper obtained through an acrylic transducer (solid line–image smoothed 3 × 3) and through the scintillator BC408 (dashed line). The scintillator profile is scaled by 0.01. (Grid line width is ~0.3 mm and linear activity is <15 kBq/cm).

The advantage of a transducer versus a scintillator is less obvious for nontransparent objects–as seen in Figs. 5 and 6, where the initial CR emission is blocked off by a screen. There is no improvement in resolution for the high-energy beta emitters due to the ring artifacts in CLI (in Fig. 6, the two rings around each sources overlap with each other at larger distances, forming a single diffuse ring). Nevertheless, for the low energy beta emitters (e.g., ^{11}C and ^{18}F), the "blind" spot should not significantly degrade image quality–these ring artifacts were not evident in our experiments with the low energy radionuclides. As can be deduced from the sharp leaf margin evident in the CLI in Fig. 9, image resolution is within a millimeter region–despite the fact that the leaf surface topology (mostly due to the vein structure) prevented direct contact between the entire surface of the leaf and the transducer. Even with this challenge, we can almost see an identical image profile between the *in vivo* image (d) and the *in vitro* image (e) of the detached leaf (after ~18 min), where the transducer had much closer contact with the leaf. This demonstrates that *in vivo* leaf CLI using a transducer can be as effective as an *in vitro* assay in estimating the radionuclide distribution in the living plant.

It should be noted that the CL image does not represent a quantitative measurement of radionuclide (such as ^{11}C) distribution in a leaf. It has been demonstrated that the quantitative measurement of beta-emitting radioactivity concentration in a thin object of nonuniform thickness (such as a leaf) can be challenging,[19,20] because beta particles may be self-absorbed by the object itself (leaf tissues) without escaping; as a result, they cannot interact with the beta detector (a plastic scintillator for typical beta imaging or a transducer for CLI in this case). Similarly, PET imaging that detects annihilation gamma rays from positron-emitting radionuclides (such as ^{11}C) is also nonquantitative when positrons annihilate in the thicker part of a leaf and escape from the thinner part of a leaf without annihilation. As a result, quantitative estimation of ^{11}C distribution in a leaf requires at least two of the following three independent measurements: distribution of the escaped beta particles from a leaf, distribution of annihilation gamma rays (or annihilated positrons) in a leaf, or the spatial variation of the thickness of a leaf. In principle, the CL image in Fig. 9 should correlate with the conventional beta image because they are both induced by the escaped positrons from the leaf surface. To derive the real activity distribution, the CI images should be corrected to the leaf thickness.

Appendix

In this appendix, we derive a simple analytical model to calculate the PSF of CLI with a transducer from beta emitters that have different emission energy spectra. We then compare the radiance profiles calculated from this model with experimental results.

From the Mott differential cross section for the Coulomb scattering of particle with energy E on angle θ

$$\frac{\mathrm{d}\sigma(\theta)}{\mathrm{d}\Omega} \sim \frac{1}{E^2 \sin^4 \theta/2}[1 - \beta^2 \sin^2 \theta/2],$$

we can see that the probability of the particle scattering on angle θ is inversely proportional to the E^2 and $\sim\theta^4$. Before a particle will be significantly deviated from its original direction, the particle undergoes a large number of interactions and loses it energy (the minimal energy for CR production in acrylic is ~170 keV). Combining this with the knowledge that most of the CR is produced by high-energy particles, we hypothesize that statistically a straight trajectory is a good approximation for the CR output estimation. It is supported by the experimental results presented in Fig. 7 where there is minimal observable radiation (<6%) from the backscattered particles when a source is placed on top of an acrylic plate facing the camera with only air in between.

Using a straight trajectory approximation, we calculated the PSFs for ^{18}F, ^{32}P and ^{76}Br. Subsequently, we calculated the CLI images' profiles of several flat uniform sources under acrylic ($n = 1.5$; 1.19 g/cm^3) transducers of different thicknesses (that were used in actual experiments) using the corresponding calculated PSF. The geometry used in the calculation is shown in Fig. 12. The calculated PSF(r) is a result of the integration over the whole emission angle (using the system symmetry we can integrate only over the polar angle dφ) and over the emission particle energy spectrum $f(E)$dE.

$$\mathrm{SF}(r) = \iint \alpha(r, \varphi, \varepsilon)\Delta W(r, \varphi, \varepsilon) f(E)\mathrm{d}E\mathrm{d}\varphi.$$

The experimental particles' energy spectra $f(E)$ were taken from the available literature[21–23] (spectra are shown in Fig. 13). ΔW is the total CR energy emitted from the element trajectory ΔL over the image (or projection) point at radius r calculated from the Frank-Tamm equation for the current particle energy ε. $\alpha/2\pi$ is the fraction of ΔW that will be detected by the imager. The current particle energy ε was calculated using the stopping power $P(E)$ from the NIST database[24] (see Fig. 14)

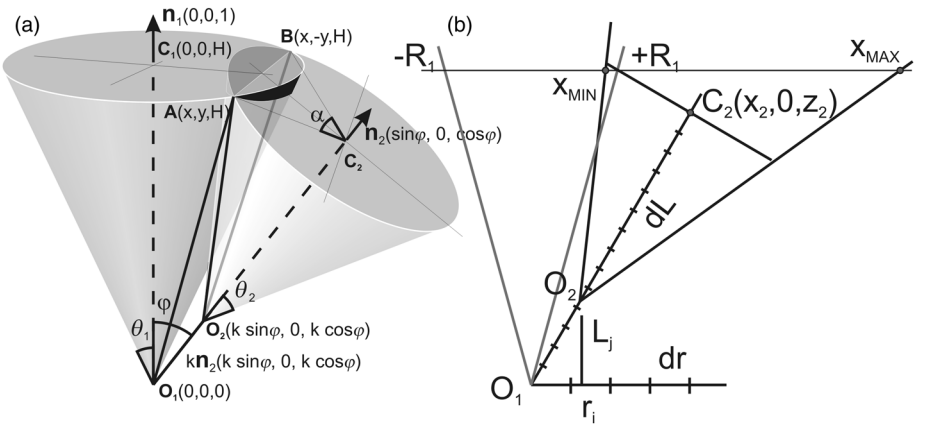

Fig. 12 (a) Point spread function (PSF) calculation geometry, and (b) its numerical representation: O_1 is a source; θ_1 is an imager aperture; C_1 is the center of the aperture ($H = |O_1C_1|$); $\mathbf{n_2}$ is the direction of the particle trajectory; k and dL are the calculation step and step size for line integrals calculations; O_2 is a current particle position $|O_1O_2| = k\mathrm{d}L$; $(O_2, \mathbf{n_2}, \theta_2)$ is a CR cone for the particle energy in point O_2; $\alpha/2\pi$ is a fraction of CR emitted by element dL from the point O_2 and detected by imager; r_i and dr are the bin number and bin size of the calculated PSF.

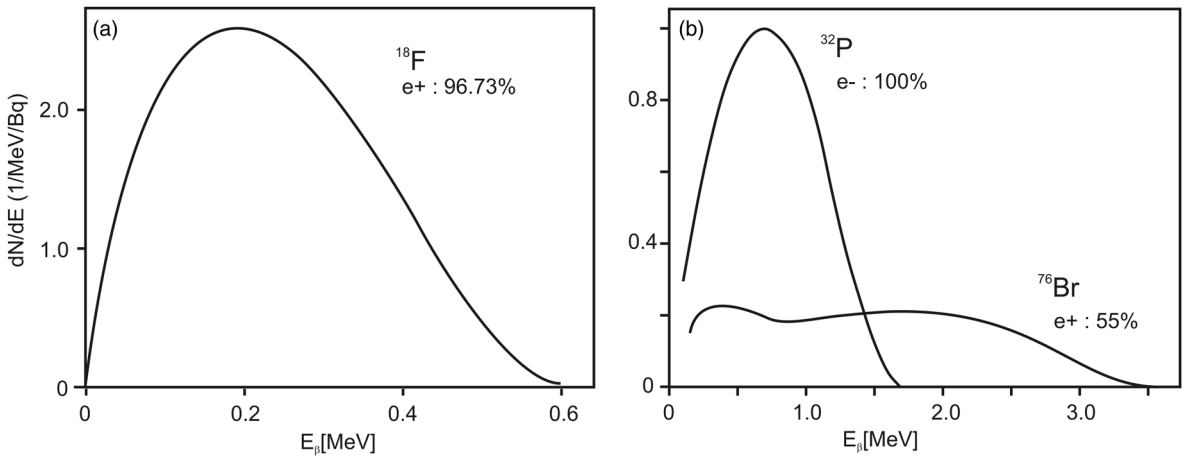

Fig. 13 The beta particle spectra for: (a) ^{18}F, (b) ^{32}P, and ^{76}Br.

$$\mathrm{d}\varepsilon = -P(\varepsilon)\rho\mathrm{d}x,$$

where ρ is the material density (1.19 g/cm^3).

The calculated profiles were compared with profiles obtained in experiments. In every experiment, we obtained three CLI images [profiles of these images are presented in Fig. 15(b)]: (1) source is on the top of the acrylic plate (thin black dotted line); (2) the same source sealed by thin (~0.04 mm) tape (thin black solid line); and (3) "flipped" source (thin black dashed line)–source on the bottom of the plate. The acrylic plate thickness was different for different

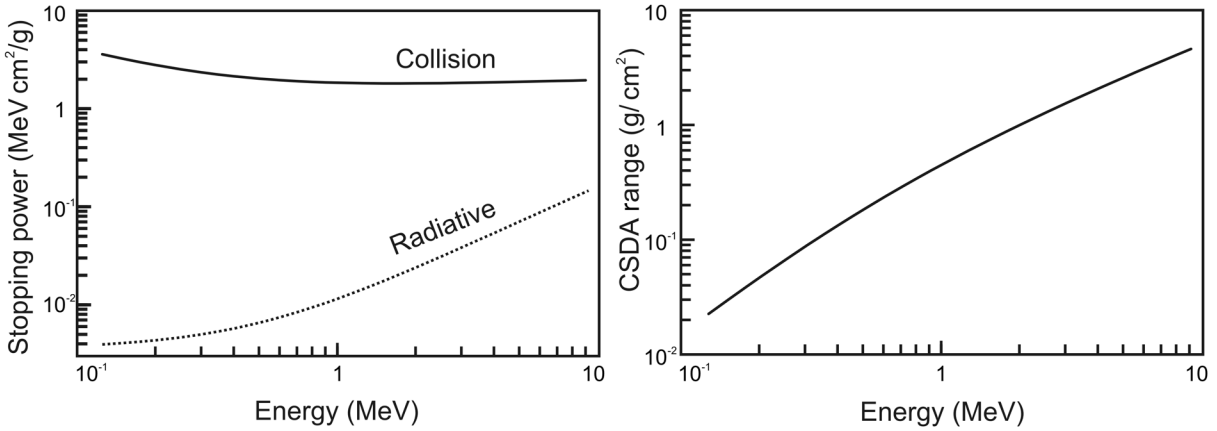

Fig. 14 Stopping power and constant slow down approximation (CSDA) range of electrons in acrylic glass.[24]

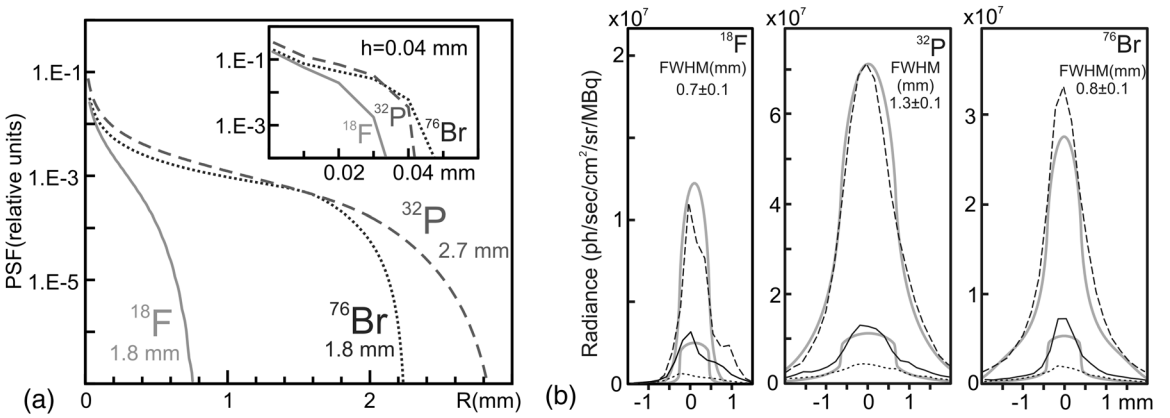

Fig. 15 (a) The calculated PSF for the acrylic transducers (transducer thickness and type of isotopes are shown in a plot); (b) gray thick solid lines are for calculated CLI profiles (large is for acrylic plate; small is for tape + 10% of calculated acrylic plate profile); thin black lines are for experimental results (dotted lines are for sources on the top of acrylic plate; solid lines are for the same source covered with tape; and dashed lines are for the "flipped" sources-source on the bottom of acrylic plate). Experimental "flipped" sources profiles are mirrored.

experiments: 2.7 mm thick for ^{32}P; and 1.8 mm for ^{18}F and ^{76}Br. The imager aperture used in the calculation (as well in the experiment) was 10 deg. The distance from the imager to the source plane was 12 cm. Assuming that the CLI of the source taken through the thin tape best represents the activity distribution, the diameters of the uniform surface sources used in calculations were selected to be equal to the FWHMs of the corresponding experimental profiles shown in Fig. 15(b) (solid black lines).

Figure 15(b) is a comparison of the radiance profiles of CL images from three radioactive sources obtained in experiments with those calculated using PSFs shown in Fig. 15(a). The gray lines are the profiles obtained using calculated PSF: the high intensity line is the flipped source radiance (CLI through thick transducer); the low intensity line is the sum of the radiance obtained from the tape-over-source calculation and 10% reflection of the flipped source profile. The results of all calculations were normalized to the max intensity of ^{32}P flipped source profile.

From these comparisons, we can draw the following conclusions: (1) the approximation of straight trajectories (statistically) works well in predicting the experimental CLI profiles. A small discrepancy between the calculation and experiment profiles can be attributed to the nonuniform activity distribution in experiments; (2) the FWHM of the calculated radiance profiles corresponds to the object size despite the large difference in beta particle energy among the three radionuclides that we tested; (3) there is approximately 10% "reflection" from the strong flashlight source (part of it can be attributed to the beta scattering); and (4) when a tape is used as the transducer, a small amount of additional light output can be seen in the shoulders of the experimental radiance profiles, possibly due to the scatter by tape of the CR light trapped inside the plate due to the total internal reflection.

Overall, we have demonstrated the feasibility of a simplified analytical model for calculating the PSF of a CL image from a clear transducer of various thicknesses using beta emitters that have a wide range of emission energy spectra. Despite the use of straight trajectory approximation to simplify the calculation, the resulted profiles show good agreement with experimentally obtained data.

Acknowledgments

This work was supported in part by the National Center for Research Resources (NCRR) of the National Institute of Health (NIH), Award No. S10RR031625; and in part by the Office of Science (BER), US Department of Energy (DOE), Grant No. DE-SC0005157 and subcontract 84900-001-10; and in part by the Mallinckrodt Institute of Radiology (Allotment 10-006). The content is solely the responsibility of the authors and does not represent the official views of the NCRR of NIH, or the BER of DOE. The authors would like to thank Lynne Jones for her help in editing the manuscript.

References

1. M. A. Lewis et al., "On the potential for molecular imaging with Cerenkov luminescence," *Opt. Lett.* **35**, 3889–3891 (2010).
2. G. S. Mitchell et al., "In vivo Cerenkov luminescence imaging: anew tool for molecular imaging," *Philos. Trans. A Math. Phys. Eng. Sci.* **369**, 4605–4619 (2011).
3. J. C. Park et al., "Luminescence imaging using radionuclides: a potential application in molecular imaging," *Nucl. Med. Biol.* **38**, 321–329 (2011).
4. G. Pratx et al., "High-resolution radioluminescence microscopy of 18F-FDG uptake by reconstructing the beta-ionization track," *J. Nucl. Med.* **54**, 1841–1846 (2013).
5. A. Ruggiero et al., "Cerenkov luminescence imaging of medical isotopes," *J. Nucl. Med.* **51**, 1123–1130 (2010).
6. A. E. Spinelli et al., "Cherenkov radiation imaging of beta emitters: in vitro and in vivo results," *Nucl. Instrum. Methods A* **648**, S310–S312 (2011).
7. A. E. Spinelli et al., "Cerenkov radiation allows in vivo optical imaging of positron emitting radiotracers," *Phys. Med. Biol.* **55**, 483–495 (2010).
8. A. E. Spinelli et al., "First human Cerenkography," *J. Biomed. Opt.* **18**, 020502 (2013).
9. A. E. Spinelli et al., "Multispectral Cerenkov luminescence tomography for small animal optical imaging," *Opt. Express* **19**, 12605–12618 (2011).
10. Antonello E. Spinelli et al., "Small animal optical multispectral Cerenkov tomography," in *Proc. Nuclear Science Symp. and Medical Imaging Conf. (NSS/MIC) 2011*, Valencia, pp. 4462–4466, IEEE (2011).
11. P. A. Čerenkov, "Visible emission of clean liquids by action of γ radiation," *Dokl. Akad. Nauk SSSR* **2**, 451–454 (1934).
12. P. A. Čerenkov, "Visible radiation produced by electrons moving in a medium with velocities exceeding that of light," *Phys. Rev.* **52**, 378–379 (1937).

13. I. M. Frank and I. E. Tamm, "Coherent radiation of fast electron in medium," *Dokl. Akad. Nauk SSSR* **14**, 107–113 (1937).
14. D. R. Froelich et al., "Phloem ultrastructure and pressure flow: sieve-element-occlusion-related agglomerations do not affect translocation," *Plant Cell* **23**, 4428–4445 (2011).
15. C. N. Topp et al., "3D phenotyping and quantitative trait locus mapping identify core regions of the rice genome controlling root architecture," *Proc. Natl. Acad. Sci. USA* **110**, E1695–E1704 (2013).
16. R. T. Clark et al., "Three-dimensional root phenotyping with a novel imaging and software platform," *Plant Physiol.* **156**, 455–465 (2011).
17. A. S. Iyer-Pascuzzi et al., "Imaging and analysis platform for automatic phenotyping and trait ranking of plant root systems," *Plant Physiol.* **152**, 1148–1157 (2010).
18. D. E. Gray, Ed., *American Institute of Physics Handbook*, 2nd ed., McGraw-Hill, New York (1963).
19. H. Wu and Y.-C. Tai, "A novel phoswich imaging detector for simultaneous beta and coincidence-gamma imaging of plant leaves," *Phys. Med. Biol.* **56**(17) 5583–5598 (2011).
20. D. L. Alexoff et al., "Pet imaging of thin objects: measuring the effects of positron range and partial-volume averaging in the leaf of Nicotiana tabacum," *Nucl. Med. Biol.* **38**(2), 191–200 (2011).
21. J. P. Blaser, F. Boehm, and P. Marmier, "The positron decay of F18," *Phys. Rev.* **75**, 1953 (1949).
22. S. C. Fultz and M. L. Pool, "Radioisotopes of bromine," *Phys. Rev.* **86**(3), 347–349 (1952).
23. E. N. Jensen et al., "The beta-spectra of P32 and P33," *Phys. Rev.* **85**(1), 112–119 (1952).
24. M. J. Berger et al., "Stopping power and range tables for electrons, positrons, and helium ions," *NIST*, http://physics.nist.gov/PhysRefData/Star/Text/ESTAR.html (2005).

Sergey Komarov is a research scientist of radiology at Washington University in St. Louis. His research focuses on the developments and applications of multimodality molecular-imaging technologies for clinical, preclinical and plant-imaging research.

Dong Zhou is an instructor of radiology at Washington University in St. Louis. His research focuses on the developments of novel radiotracers and radiolabeling techniques for molecular-imaging applications.

Yongjian Liu is an assistant professor of radiology at Washington University in St. Louis. His research focuses on the development of nanotechnologies and novel radiopharmaceuticals for both preclinical and clinical diagnostic and therapeutic applications.

Yuan-Chuan Tai is an associate professor of radiology and biomedical engineering at Washington University in St. Louis. His research focuses on the development and applications of multimodality molecular-imaging technologies for clinical, preclinical and plant-imaging research.